ACS APPLIED MATERIALS & INTERFACES

www.acsami.org

Research Article

# Wearable Capacitive Pressure Sensor Based on MXene Composite Nanofibrous Scaffolds for Reliable Human Physiological Signal Acquisition

Sudeep Sharma, Ashok Chhetry, Md Sharifuzzaman, Hyosang Yoon, and Jae Yeong Park*

Cite This: *ACS Appl. Mater. Interfaces* 2020, 12, 22212–22224

Read Online

ACCESS | Metrics & More | Article Recommendations | Supporting Information

**ABSTRACT:** In recent years, highly sensitive pressure sensors that are flexible, biocompatible, and stretchable have attracted significant research attention in the fields of wearable electronics and smart skin. However, there has been a considerable challenge to simultaneously achieve highly sensitive, low-cost sensors coupled with optimum mechanical stability and an ultralow detection limit for subtle physiological signal monitoring devices. Targeting aforementioned issues, herein, we report the facile fabrication of a highly sensitive and reliable capacitive pressure sensor for ultralow-pressure measurement by sandwiching MXene ($Ti_3C_2T_x$)/poly(vinylidene fluoride-trifluoroethylene) (PVDF-TrFE) composite nanofibrous scaffolds as a dielectric layer between biocompatible poly-(3,4-ethylenedioxythiophene) poly-styrene sulfonate /polydimethylsiloxane electrodes. The fabricated sensor exhibits a high sensitivity of 0.51 $kPa^{-1}$ and a minimum detection limit of 1.5 Pa. In addition, it also enables linear sensing over a broad pressure range (0−400 kPa) and high reliability over 10,000 cycles even at extremely high pressure (>167 kPa). The sensitivity of the nanofiber-based sensor is enhanced by MXene loading, thereby increasing the dielectric constant up to 40 and reducing the compression modulus to 58% compared with pristine PVDF-TrFE nanofiber scaffolds. The proposed sensor can be used to determine the health condition of patients by monitoring physiological signals (pulse rate, respiration, muscle movements, and eye twitching) and also represents a good candidate for a next generation human−machine interfacing device.

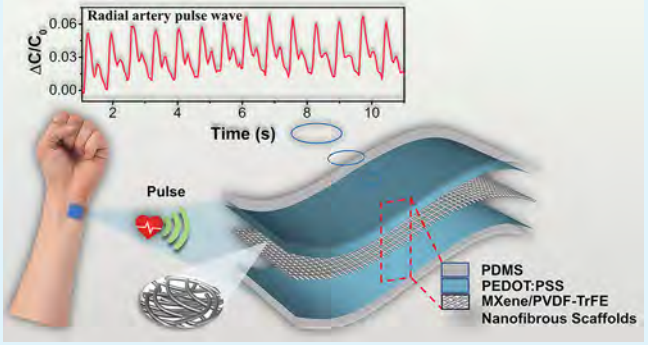


**KEYWORDS:** *MXene/PVDF-TrFE, wearable sensor, composite nanofiber, capacitive pressure sensor, physiological signal monitoring*



## 1. INTRODUCTION

Recently, emerging studies about wearable pressure sensors have attracted substantial research interest because of their colossal multifunctional potential for application in intelligent robotics, flexible touch screens, smart electronic skin, physiological signal monitoring, and human−machine interface.[1−5] The fundamental principle of a pressure sensor is to transduce the change in an external force to a recognized signal by exploiting various sensing mechanisms, which include capacitive,[5−7] triboelectric,[8] piezoresistive,[9−11] piezoelectric,[12] and transistors[13] methods. Among these sensing mechanisms, the capacitive pressure sensor (CPS), realized by a force-induced capacitance change, has aroused a great deal of research interest because of its facile and low-cost fabrication, high stability, fast response time, and low power consumption. Although evolving research paths in pressure sensors have shown progressive results in the field of flexible electronics,[14−20] there still exist critical challenges to simultaneously achieve a high sensitivity over broad pressure range and long term stability even under the extremely high-pressure condition for comprehensive biosignal monitoring ranging from small deformations (pulse rate, respiration, and phonation detection) to large deformations (muscles movement, arm, and knee bending).

The sensing performance of the flexible CPS is based on the principle of a parallel plate capacitor and is calculated by $C = \varepsilon A/d$, where $\varepsilon$, $A$, and $d$ represent the dielectric constant, the overlapping area between the electrodes, and the distance between the two electrodes, respectively.[24] For a fixed overlapping area, by applying an external force, a change in capacitance can be observed by the deformation of dielectric material either by changing the value of "$\varepsilon$" or "$d$" or both. Because sensitivity is well defined as the change in relative capacitance for change in applied pressure, increasing dielectric

Received: March 29, 2020
Accepted: April 17, 2020
Published: April 17, 2020




https://dx.doi.org/10.1021/acsami.0c05819
*ACS Appl. Mater. Interfaces* 2020, 12, 22212−22224

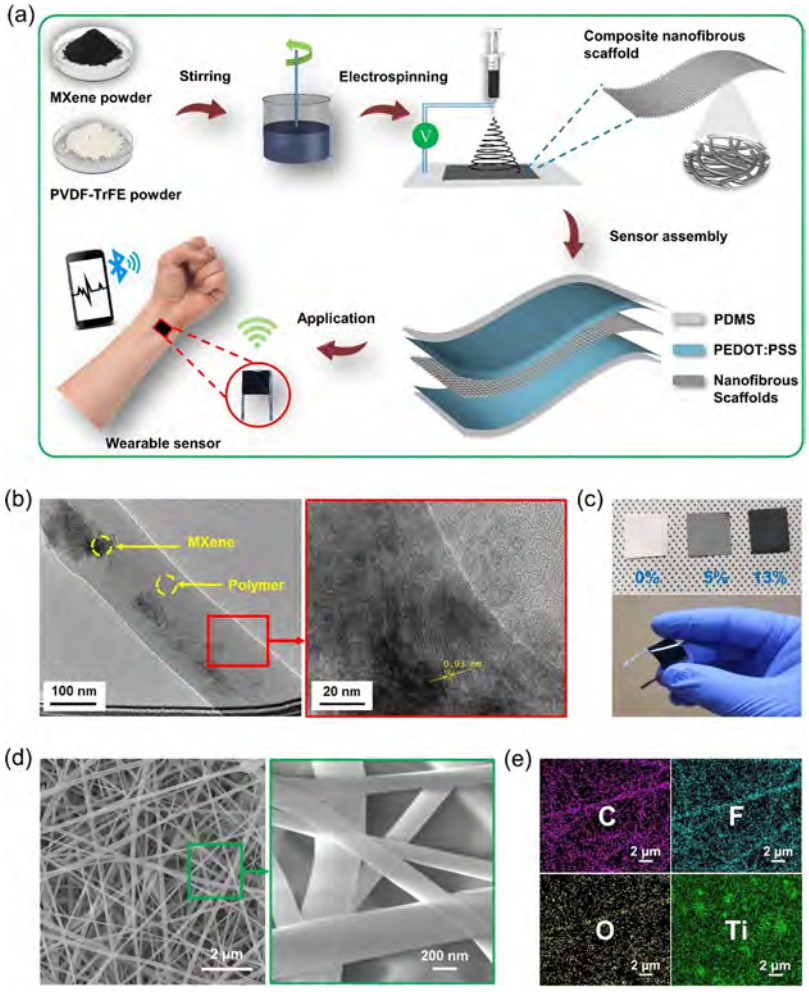


**Figure 1.** Fabrication sequence and structure of the CNS-based pressure sensor. (a) Schematic diagram demonstrating the fabrication of the CNS-based pressure sensor. (b) TEM image of the CNS, showing single-layer and multi-layer MXene nanoflakes. The inset displays high-resolution TEM, showing the interlayer spacing of 0.93 nm corresponding to the (002) plane of MXene. (c) Photographs showing the CNS with different MXene concentrations and the fabricated sensor. (d) FESEM image of the CNS and the inset show the morphology at a higher magnification. (e) EDS maps of the composite nanofibers showing C, F, O, and Ti elements.

constant change or reducing compressive modulus of the dielectric layer is a crucial factor to achieve high sensitivity for a CPS.[25] Thus, several flexible CPSs with unique structural designs have been proposed by changing the conformation of the dielectric layer to reduce modulus and achieve high sensitivity, which includes the construction of a microstructure elastomer,[26] microstructures intronic film,[27] or nanofiber scaffolds.[28] The use of air void structures on the dielectric layer is an effective way to reduce the compressive modulus of the material, thereby enhancing the resulting sensitivity of CPS. The use of microstructured elastomers or film has shown enhanced sensitivity (0.3−0.7 $kPa^{-1}$)[21−23] because the fabrication of the microstructures decreases the stiffness of the material, resulting in greater deformation of the dielectric layer. However, the fabrication of microstructured dielectric requires a very expensive and complicated photolithography process.[21,26] Therefore, a simple and cost-effective fabrication process of highly deformable nanofiber scaffolds provides a high specific surface area, high pore volume, adequate porosity, and low modulus in comparison to microstructure dielectric sensors.[29,30] The combination of these characteristics provides this material great potential to be applied in the field of capacitive pressure sensing applications.[31,32] However, a nonuniformity in the diameter, random alignment, and mechanical stiffness of polymer fibers hinder the performance of the target device when used as a sensing material. Concomitant to these facts, encompassing nanofillers can truly optimize and reinforce nanofibers by improving their thermal and electrical conductivities and mechanical and dielectric properties.[33−38] Conductive nanofiller materials, such as carbon nanotubes (CNTs),[39−41] silver nanowires,[42−44] graphene,[45−47] MXene,[48−50] and nanodiamonds,[51] have been frequently used to reinforce nanofibers by enhancing their inherent properties. Recently, Mu et al.[52] demonstrated a CPS with a $CaCu_3Ti_4O_{12}$ composite sponge, which showed a high sensitivity (1.66 $kPa^{-1}$) in the low-pressure range. However, the CPS of the reported work possessed poor stability introduced from a distorted response, making the device incompatible to be used in the ultralow-pressure range. Zhan et al.[2] and Guo et al.[4] fabricated a wearable pressure sensor for physiological signal monitoring using tissue paper-embedded nanoparticles as a sensing element, which exhibited high sensitivity for a broad pressure range. On the other hand, the fabricated wearable device showed poor durability performance even under very low pressure (<3 kPa), making the device susceptible to high noise in the low-pressure range.


https://dx.doi.org/10.1021/acsami.0c05819
ACS Appl. Mater. Interfaces 2020, 12, 22212−22224

Furthermore, Wang et al.[28] fabricated carbonized silk nanofibers for application in a pressure sensor, which showed an ultralow detection limit of 0.8 Pa and excellent sensitivity (34.47 $kPa^{-1}$). However, the carbonization process is time-consuming and expensive, which proves to be difficult for large-scale fabrication. Therefore, there remains a huge challenge to develop a highly sensitive and stable sensor with a facile fabrication technique.

Liu et al.[53] fabricated a pressure sensor utilizing a CNTs/cotton textile and achieved a high sensitivity of 14.4 $kPa^{-1}$. However, one-dimensional (1D) materials offer a low surface area and can easily accumulate into bundles, which result in a nonuniform dispersion in the textile matrix that degrades the mechanical properties of the sensing material. Thus, replacing a 1D material by a two-dimensional (2D) material can resolve the problem regarding uniform dispersion by providing a large surface area and enhanced adhesion. A newly discovered 2D class of metal carbonitrides and carbides, called MXenes ($Ti_3C_2T_x$), was synthesized after exfoliating from the MAX phase ($Ti_3AlC_2$) by selectively etching the A-layers from its precursor $M_{n+1}AX_n$.[54] The characteristics of MXenes include a high specific capacitance and thermal stability, excellent mechanical properties, surface functional groups (−O, −F, −OH), and ion intercalation.[55−57] These features make MXenes a promising entrant for supercapacitor applications,[58] gas sensing applications,[59] electromagnetic interface shielding,[60] and energy harvesting applications.[61] Although MXenes possess great physical and chemical properties, very few studies have reported the properties and application of MXene/polymer composite nanofibers.[34,50,61] To the best of our knowledge, there are no reports regarding the fabrication of a pressure sensor using MXene composite nanofibrous scaffolds (CNS). However, a substantial need exists for the production of biocompatible and environmentally friendly electrodes for healthcare monitoring. The brittleness, low conductivity, and high cost of indium tin oxide (ITO), traditionally used as an electrode material for sensors,[26,62,63] limit device performance in terms of flexibility and conductivity. Therefore, various materials, including nanotubes,[64] conductive nanoparticles,[7] nanowires,[27] and poly-(3,4-ethylenedioxythiophene) polystyrene sulfonate (PEDOT:PSS)[65] have been recently used as an alternative to ITO. Among them, PEDOT:PSS has attracted great attention in the field of organic electronics because of its tunable electrical conductivity, decent biocompatibility, high mechanical stretchability, and high stability under ambient conditions.[64,66,67]

In this paper, an CNS is newly developed using an efficient and facile fabrication technique. The proposed all-polymer CPS with an ultralow pressure detection limit and a highly stable over broad pressure range is designed and fabricated by sandwiching the CNS, as a dielectric layer, between PEDOT:PSS/polydimethylsiloxane (PDMS) electrodes. The polymer PVDF-TrFE fiber scaffolds are preferred because of its excellent mechanical strength and resilience, high dielectric constant, and reliably maintainance of a specific electrospun fiber scaffold thickness. The MXene is added to increase the dielectric constant and reduce the compression modulus, thus, to enhance the sensing properties of the fabricated sensor. While previous wearable pressure sensors exhibit narrow range, nonlinear stability cycles, and high signal distortion in the low-pressure application, the proposed sensor can maintain stable response with minimal hysteresis even under high stress (>167 kPa), which can be an impeccable candidate for long-term functioning and reliable for ultralow pressure applications. For proof-of-concept, the fabricated sensor is characterized and evaluated by monitoring various human physiological signals, ranging from small to large deformations, suggesting viable applications in biomedical informatics, medical diagnosis, and next-generation human−machine interfacing devices.

## 2. RESULTS AND DISCUSSION

**2.1. Fabrication and Structure of the Sensor.** Figure 1a illustrates a schematic of the fabrication method for the CNS-based pressure sensor. A 2D metal carbide, MXene, was blended with a PVDF-TrFE, and CNSs were primed as a dielectric material by an electrospinning process. To determine the optimized thickness, the CNSs were prepared for various spinning times while keeping all other spinning parameters constant (see the Materials and Methods section for details) for all the samples. However, to determine the best thickness of the CNS, the spinning time was controlled. The as-prepared CNS was sandwiched in between PEDOT:PSS/PDMS films. For more details about electrode and sensor fabrications, see Figure S1, Supporting Information and the Materials and Methods section, respectively. Before using PEDOT:PSS for the top and bottom electrodes, the solution was cross-linked with divinyl sulfone (DVS) to make the films mechanically robust and stretchable.[68] Subsequently, each film was post-treated with the polar solvent dimethyl sulfoxide (DMSO), which decreased the sheet resistance to ∼2.2 Ω $sq^{-1}$ (Figure S2, Supporting Information) because of removal of PSS nonconductive polymer chains.[67] The nanofiber morphology was studied by transmission electron microscopy (TEM), as shown in Figure 1b, which reveals the presence and orientation of single to few layers of MXene flakes encapsulated inside the PVDF-TrFE nanofiber of ∼200 nm diameter without affecting the fiber uniformity. The insets display a high-resolution TEM image of MXene with nanoflake size 2−7 nm and an interlayer spacing of 0.93 nm corresponding to (002) plane of MXene.[69] The detail TEM analysis of nanofibers is shown in Figure S3, Supporting Information. Figure 1c (top) shows a photograph of the CNS at different MXene concentrations, which reveals that the fabricated electrospun scaffolds of pure PVDF-TrFE is thin and flexible, and on account of the addition of MXene, it appears darker compared to pure MXene/PVDF-TrFE. The photograph of Figure 1c (bottom) depicts the fabricated sensor, showing its flexibility. Figure 1d is the field-emission scanning electron microscope (FESEM) image of the CNS; the inset shows a magnified view of the nanofibers, with a diameter of ∼400 nm, demonstrating that CNSs were successfully produced with highly porous 3D network structures. Figure 1e depicts the energy dispersive spectrometer (EDS) mapping images of the CNS, manifesting the uniform dispersion of C, F, O, and Ti throughout the nanofibers, which are components of the PVDF-TrFE and MXene. Thus, the EDS image concludes that MXene nanosheets are uniformly distributed throughout the CNS.

**2.2. Materials Characterization.** *2.2.1. MXene.* The MXene was synthesized using a method similar to that reported in the previous article.[45] This approach includes exfoliating $Ti_3AlC_2$ by an etchant (HCl/LiF) and removing the Al layers from it, and then, the exfoliated multilayer $Ti_3C_2T_x$ was delaminated by sonication in an ice bath. The cross-sectional FESEM image of the MXene nanosheets of Figure S4, Supporting Information, reveals that the aluminum layer was etched away and the MXene nanosheets were properly


https://dx.doi.org/10.1021/acsami.0c05819
ACS Appl. Mater. Interfaces 2020, 12, 22212−22224

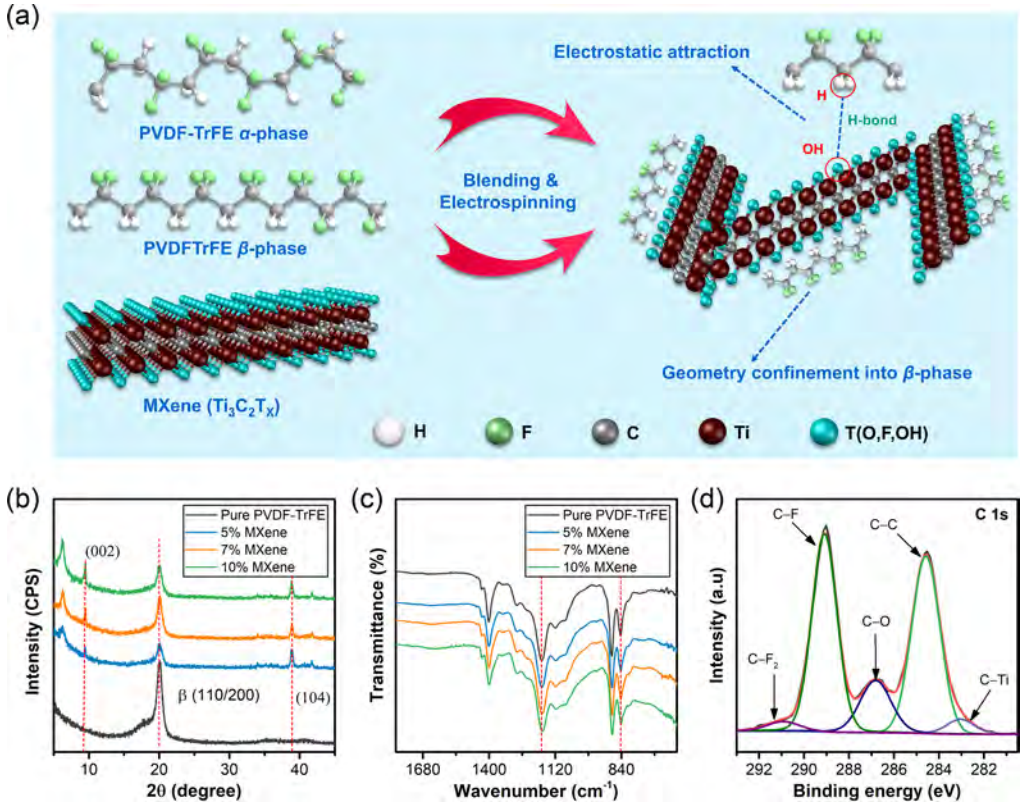


**Figure 2.** Schematic illustration and surface characterization of the CNS. (a) Schematic illustration showing the synergistic effect obtained after the MXene is introduced into the polymer matrix. (b,c) XRD and FTIR analyses of CNS with various MXene concentrations. (d) XPS spectrum of the C 1s region of the CNS with 5 wt % MXene concentration.

delaminated. Additionally, the X-ray diffraction (XRD) analysis (Figure S5a, Supporting Information) shows a strong peak (002) at $2\theta = 9°$, which confirms the successful synthesis of the MXene. The Raman spectrum (Figure S5b, Supporting Information) indicates a peak at 399 $cm^{-1}$, which is assigned to the $B1_g$ mode, and three $E_g$ mode peaks centered around at approximately 128, 280, and 620 $cm^{-1}$ representing the vibrational modes of $Ti_3C_2F_2$, $Ti_3C_2(OH)_2$, and $Ti_3C_2F_2$, respectively.[36] The peaks confirm the presence of functional groups (−F, −OH, and −O) on the surface of the MXene. Additionally, peaks at 1391 and 1596 $cm^{-1}$ correspond to the D-and G-bands, respectively, which illustrate the presence of amorphous carbon in the MXene.[70] Furthermore, X-ray photoelectron spectroscopy (XPS) of the MXene was performed to quantify the surface functionalities of the materials. The detailed survey spectrum analysis of the MXene (Figure S6a, Supporting Information) depicts the existence of Ti, F, C, and O. Furthermore, there is no Al present in the MXene, assuring the successful etching of the MAX phase ($Ti_3AlC_2$). In addition, the presence of O and F indicates the formation of the surface functional groups $-OH(Ti_3C_2(OH)_2)$ and $-F(Ti_3C_2F_2)$ during etching reactions.[36] The high-resolution XPS spectrum of the C 1s (Figure S6b, Supporting Information) reveals core level peaks located at 281.7, 283.70, 284.92, 286.42, and 288.60 eV corresponding to C−Ti, C−Ti−O, C−C/C−H, C−O, and C−F/O−C═O bonds.[71]

*2.2.2. Composite Nanofiber.* The CNS was prepared by blending the MXene and PVDF-TrFE, followed by the electrospinning process. During the process of mixing and spinning, two kinds of effects can be observed. First, the van der Waals attractive force occurs because of the electrostatic attraction between H or F atoms (existing in the PVDF-TrFE polymer) and functional groups (existing in the MXene).[36] Second, the transition from $\alpha$-phase crystallization to $\beta$-phase crystallization,[72] which overall synergistically modifies the fiber mechanical properties. The above statements are further illustrated and supported by the schematic in Figure 2a and the physical characterizations [XRD, Fourier-transform infrared spectroscopy (FTIR), and XPS]. Figure 2b shows the XRD analysis of the CNS and indicates the presence of several peaks when the MXene was incorporated inside the neat polymer matrix. All the composite samples exhibit a strong and prominent (002) and (104) planes around 9 and 39°, respectively, which are derived from the MXene sheets.[36] As the filler concentration increases, the interlayer spacing associated with the (002) diffraction peaks expand (Figure S7a, Supporting Information), which suggests the intercalation of polymer chains between MXene layers; this action can be assisted *via* the H and F atoms of PVDF-TrFE polymer chains and the functional groups of the MXene surface.[36] Furthermore, the (002) diffraction plane of the MXene greatly enhanced with the increase in filler concentration in the polymer. However, the $\beta$-characteristics (110/200 planes) are largely suppressed (Figure S7b, Supporting Information), which indicates a negative influence of the nanofillers on the $\beta$-crystallinity of the PVDF-TrFE polymer. This result suggests that the incorporation of the MXene nanofiller can hinder the crystallinity of the PVDF-TrFE main chain instead of supporting cocrystallization with the MXene.[73] This concept is further supported by the FTIR spectra of the composite fibers (Figure 2c). The intensity of the absorption bands (840


https://dx.doi.org/10.1021/acsami.0c05819
ACS Appl. Mater. Interfaces 2020, 12, 22212−22224

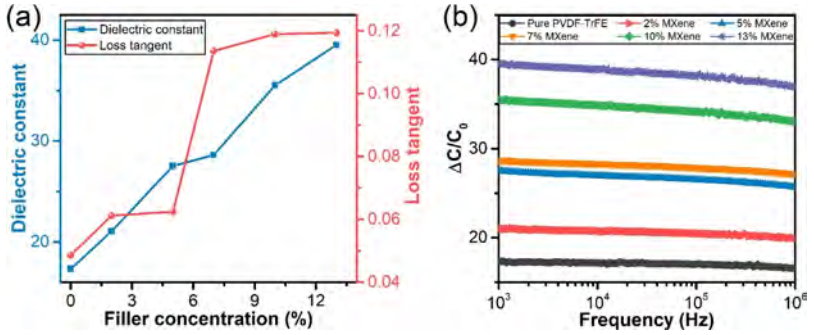


**Figure 3.** Electrical characterizations of different samples. (a) Dielectric constant and loss tangent of CNS with respect to the MXene content in wt %. (b) Frequency dependence of the dielectric constant.

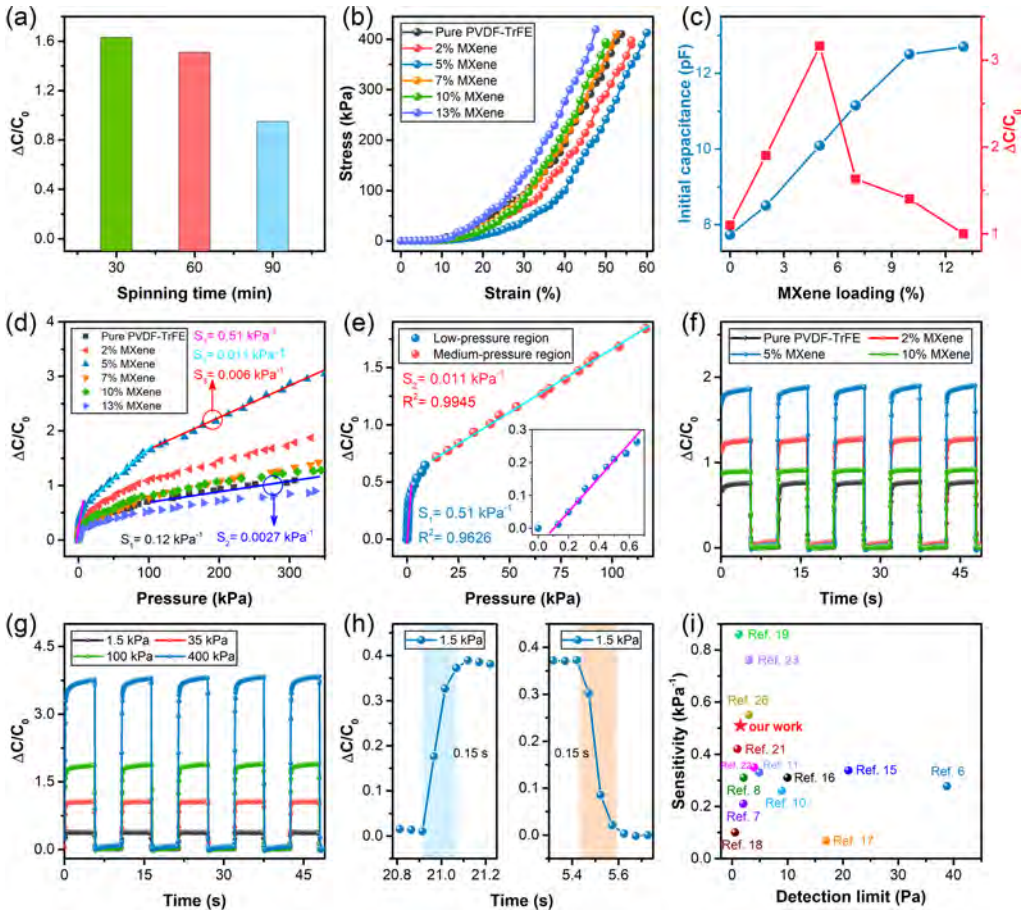


**Figure 4.** Electromechanical characterization of the CNS-based pressure sensor. (a) Performance comparison of the CNS-based sensor based on different electrospinning times. (b) Compressive stress−strain performance of the sensor for a steady loading of up to 0.4 mm compression distance. (c) Dependence of the initial capacitance ($C_0$) and the relative change in capacitance ($\Delta C/C_0$) of the CNS-based sensor on the MXene content in wt %. (d) Relative capacitance change ($\Delta C/C_0$) of the CNS-based sensors with dielectric layers having different MXene concentrations in wt %, under a constant compression distance of 0.4 mm. (e) Descriptive plot of $\Delta C/C_0$ illustrating the pressure sensitivity attained with the 5 wt % MXene loading. The inset shows the sensitivity of the sensors in the low-pressure region. (f) Cyclic capacitive response of the CNS-based sensor (loading/unloading) under a constant compression distance of 0.3 mm for different MXene concentrations and (g) cyclic capacitive response of the CNS-based sensor with a 5 wt % MXene concentration under different loading/unloading pressure values. (h) Response and relaxation time for a loading/unloading cycle with a pressure of 1.5 kPa. (i) Performance of the sensor in terms of sensitivity reported at a low-pressure range with a low detection limit compared to those of previous reports.

and 1290 $cm^{-1}$) corresponding to the $\beta$-crystal plane is reduced after introducing the MXene into PVDF-TrFE. A possible explanation to support this result is that the demolition of C−H and C−F bonds creates an imbalance in the $\beta$-(TTT conformations), which results in the reduced crystalline properties of the CNS.[73] In addition, for all concentrations, the FTIR spectra contain familiar peaks similar with those of the pure PVDF-TrFE polymer, and no additional peaks are present. However, a decrease in the transmittance is observed as the filler concentration increases. Figure 2d exhibits the high-resolution XPS spectrum of the C 1s region that can be fitted with five component peaks centered at


https://dx.doi.org/10.1021/acsami.0c05819
ACS Appl. Mater. Interfaces 2020, 12, 22212−22224

283.04, 284.58, 286.82, 289.09, and 290.92 eV, corresponding to C−Ti, C−C, C−O, C−F, and C−$F_2$, respectively. The MXene introduces new bonds in the carbon chain (C−Ti and C−O), which suggests that the presence of oxygen (−O) and titanium (−Ti) terminated groups in the polymer chain structure alters the original carbon chain conformations.[74] For the detailed XPS analysis of the CNS, refer to Figure S8, Supporting Information.

**2.3. Electrical Characterization.** The dielectric constant and loss tangent of the CNS as a function of loading concentration is shown in Figure 3a, which reveals trends for both the dielectric constant and loss tangent that follow the increase in the filler concentration. For the rising filler concentration (0−13 wt %) in the polymer fiber matrix, the dielectric constant ($\varepsilon_r$) increases initially from 10 to 40, and similarly, dielectric loss also increases (from 0.05 to 0.12) up to the maximum filler concentration. The $\varepsilon_r$ of the CNS, with various concentrations of the MXene, as a function of the frequency range ($10^3$ to $10^6$ Hz), is presented in Figure 3b, which depicts a significant increase in $\varepsilon_r$ of approximately four times that of the pure PVDF-TrFE. This enhanced dielectric performance can be explained by two different phenomena: microscopic dipole formation and microcapacitor network formation.[36,75] These mechanisms provide considerable contribution to the increase in the dielectric constant. As the frequency increases, a decreasing trend in $\varepsilon_r$ can be observed at high filler concentrations, which can be attributed to tunneling charge injection and an increased leakage current as the MXene nanosheets are situated very close to each other at high concentrations.[76] Furthermore, the dielectric loss increases with the filler concentration (Figure S9a, Supporting Information), which is due to the upsurges in the microcapacitor formation and the conductive path network. In addition, the frequency dependence of the ac conductivity for different-concentration CNSs is demonstrated in Figure S9b, Supporting Information, and indicates an insulating behavior in the low-frequency range (below $10^5$ Hz) and a conducting nature at high frequencies (beyond $10^5$ Hz), which are proportional to the filler concentration. The conclusion is that at high frequency, conductive filler forms a conductive steady percolation bridge throughout the polymer matrix.[76]

**2.4. Electromechanical Characterization.** The performance of the CPS as a factor of the thickness of the dielectric nanofiber scaffolds was investigated by varying the thickness (electrospinning time) while keeping all other parameters (voltage, rate of injection, needle-collector distance, and spinning area) constant, as shown in Figure 4a (see the Materials and Methods section for details). Three CNS with 2 wt % MXene were prepared corresponding to spinning times of 30, 60, and 90 min. To find the optimized thickness, the relative change in capacitance was evaluated by applying a constant pressure of 400 kPa to each CNS. The CPS with the thinnest dielectric layer, which corresponds to a shorter spinning time, exhibits a relative change in capacitance ($\Delta C/C_0$) that is higher than that of the thickest dielectric layer, corresponding to a longer spinning time. For example, the CNS electrospun at 30 min has a $\Delta C/C_0$ of 1.65, which is substantially greater than that of the CNS spun at 60 and 90 min. The large increase in the $\Delta C/C_0$ of the thinnest dielectric layer can be understood by considering that the thin CNS exhibits a large porous structure allowing for large deformation of the dielectric layer.[77] Figure 4b presents the compressive stress−strain curves for the CNS-based sensor with different MXene concentrations, which reveal that the compression modulus decreases by 58% as the content of MXene increases to 5% (e.g., at the instance of 31.5 strain %, pure PVDF-TrFE shows compression modulus of 3.5, which decreased to 1.45 for 5% MXene concentration). However, there is a noticeable increase in the modulus with further increments in the MXene concentrations. Interestingly, the compression modulus decreases by 58% at a 5% filler concentration, which can be explained by two principles: the decrease in crystallinity and the increase in the free volume of the polymer matrix. First, the addition of the MXene might have decreased the mobility of the polymer chain during electrospinning, which can indeed decrease the crystallinity of the nanofiber. As the $\beta$-(TTT conformation) of the nanofiber carbon chain changes, the polymer crystallinity may be reduced, which softens the polymer fiber and, in turn, decreases the compression modulus compared to that of the pure PVDF-TrFE nanofiber scaffolds (see the detailed explanation in the XRD analysis).[73] Second, the mixing of nanoparticles with polymers is often not perfect and can introduce a certain free volume between polymer chains. With more free volume, the polymer chains can more easily pack close to each other, resulting in a low compression modulus.[78] However, for the filler concentrations higher than 5%, the interparticle space can decrease and the nanofillers begin to agglomerate inside the nanofiber. This agglomeration may cause the interphase material around the nanofibers to create a 3D physical network in the polymer matrix overcoming the free volume effect.[79] Beyond the 5% concentration of MXene, this phenomenon increases the compression modulus of the CNS. Figure 4c shows $C_0$ and $\Delta C/C_0$ as functions of the MXene loading. As indicated in the figure, the $C_0$ of the CNS-based sensor gradually increases (7.5−12.5 pF) with the MXene concentration. However, the tendency of $\Delta C/C_0$ reveals a rapid increase at first, reaching a maximum of 3.25 at 5% MXene and then a steady decrease until the value reaches 1.1 at the highest filler concentration (13%). The rise in the initial capacitance is because of the dielectric permittivity enhancement. As the capacitance is directly proportional to the dielectric permittivity, the addition of a nanofiller to the polymer matrix increases the formation of a microcapacitor network, which in turn raises the dielectric permittivity and initial capacitance of the sensor. In addition, the changing trend observed in $\Delta C/C_0$ can be explained with the compression stress−strain analysis: the lower the compression modulus is, the higher the deformation of the dielectric layer because of the softening of the dielectric material, which increases the value of $\Delta C/C_0$. Conversely, the higher the compression modulus is, the more rigid the dielectric material becomes, which decreases the value of $\Delta C/C_0$. Figure 4d presents the relative change in capacitance under a compression distance of 0.4 mm for all the concentrations. The sensitivity ($S$) is defined as $S = (\Delta C/C_0)/P$, where $\Delta C/C_0$ indicates the relative change in capacitance and $P$ is the applied pressure. A pressure sensor with the 5% MXene concentration exhibits the highest sensitivity, in comparison to that of other concentrations, for all pressure ranges. For example, the sensitivities of a CNS-based sensor with 5% MXene are 0.51 $kPa^{-1}$ for the low-pressure range (0−1 kPa), 0.01 $kPa^{-1}$ for the medium-pressure range (10−150 kPa), and 0.006 $kPa^{-1}$ for high-pressure range (150−400 kPa). In comparison, the sensitivities of the CNS-based sensor with pristine PVDF-TrFE are 0.12 and 0.0027 $kPa^{-1}$ for the low- and high-pressure ranges, respectively. The


https://dx.doi.org/10.1021/acsami.0c05819
ACS Appl. Mater. Interfaces 2020, 12, 22212−22224

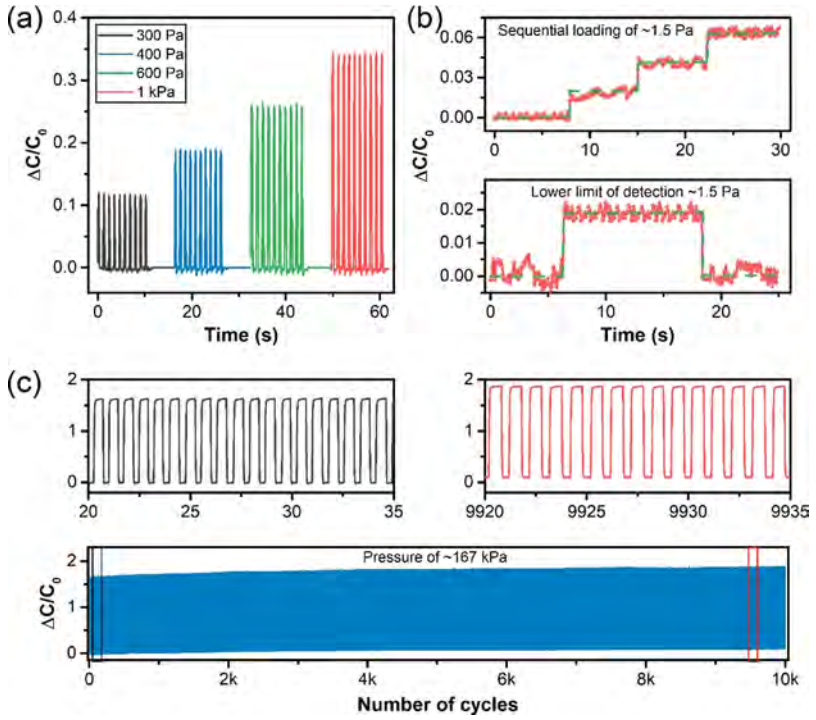


**Figure 5.** (a) Relative change in capacitance response under low-pressure loading and unloading cycles. (b) Demonstration of the lower limit of detection by sequential loading and unloading of a long grain of rice equivalent to ~38 mg. (c) Cyclic stability test of the CNS-based pressure sensor over 10,000 loading and unloading cycles under (>40% compression) a high-pressure of ~167 kPa. The insets present selected cycles at the beginning and end of the stability test.

high sensitivity induced by the 5 wt % MXene loading can be explained with the plot from the compressive stress−strain analysis and the dielectric constant dependence on the concentration of the MXene. The compression modulus of the CNS decreases with the filler concentration up to 5% and softens the polymer nanofibers providing for a larger and easier deformation, even for very low stress. Consequently, a lower compression modulus helps to increase the sensitivity of the pressure sensor. In addition, higher change in relative dielectric permittivity also increases the sensitivity by increasing the relative change in capacitance because the relative change in capacitance is directly related to change in relative permittivity of the material ($\varepsilon_r/\varepsilon_{r0}$).[25] In CNS, the relative permittivity is the composition of the air, MXene, and polymer. As shown in Figure S10 (Equation S1, Supporting Information), under certain pressure, the thickness of the dielectric material changed from $d_0$ to $d_0'$ and the low permittivity air voids were replaced by the combination of high permittivity of MXene and PVDF-TrFE, leading to an enhanced dielectric permittivity, which consequently increased its capacitance change and the sensitivity of the device.[52] However, beyond the 5% MXene concentration, the compression modulus starts to increase, which results in the nanofibers to become stiffer and decreases the sensitivity. Figure 4e depicts a more illustrative view of the pressure sensitivity for 5% MXene, showing a remarkable sensitivity of 0.51 $kPa^{-1}$ with a linear fit of $R^2$ = 0.9626 in the low-pressure region (<1 kPa) and 0.01 $kPa^{-1}$ with 0.9945 in the medium-pressure region (>10 kPa). In the low-pressure range, even a low applied force can induce a large deformation in the nanofiber because highly porous and soft CNSs are prone to low pressure, which induces a greater change in the capacitance, and as a result, high sensitivity is achieved. Similarly, in the medium pressure range, the effect is induced because of the compression of soft polymer nanofibers and few air voids inside the nanofiber scaffolds, which results in comparatively less sensitivity than the low-pressure range. However, in the high-pressure range, the deformation of the CNS almost saturated, due to decreased porosity, increased stiffness of the polymer nanofiber, the sensitivity becomes compromised. The capacitive response for cyclic loading/unloading was investigated with a compression distance of 0.3 mm for all of the samples and is plotted in Figure 4f. Among all other concentrations, the sensor with the 5% MXene concentration exhibits a high $\Delta C/C_0$, which can be due to the higher sensitivity of the 5% MXene composite in the high-pressure and low-pressure ranges. Thus, the 5% CNS was considered for further electromechanical characterization and targeted applications because of its superior performance. To investigate the wide detection range and reliability of the CNS-based sensor, the device was subjected to dynamic loading/unloading at different pressures (Figure 4g). There is an abrupt transition in the response during each loading and unloading of the pressure, while the response is stable during no transition; also, the capacitance response of the sensor is linear with pressure. The data conform with the notion that the fabricated sensor can evidently detect different pressure levels and small-large deformations, with a stable and hysteresis-free response. The response and relaxation times of the fabricated sensor were evaluated under a 1.5 kPa pressure, which corresponds to 1 mm compression, as shown in Figure 4h. As seen from the figure, equal dynamic response and relaxation times (0.15 s) were observed, which indicates that the time for the elastic recovery of the CNS is the same as that of compression, depicting no hysteresis. The performance of the CNS-based sensor in terms of sensitivity in the low-pressure range and the low detection limit is compared with those from recently


https://dx.doi.org/10.1021/acsami.0c05819
ACS Appl. Mater. Interfaces 2020, 12, 22212−22224

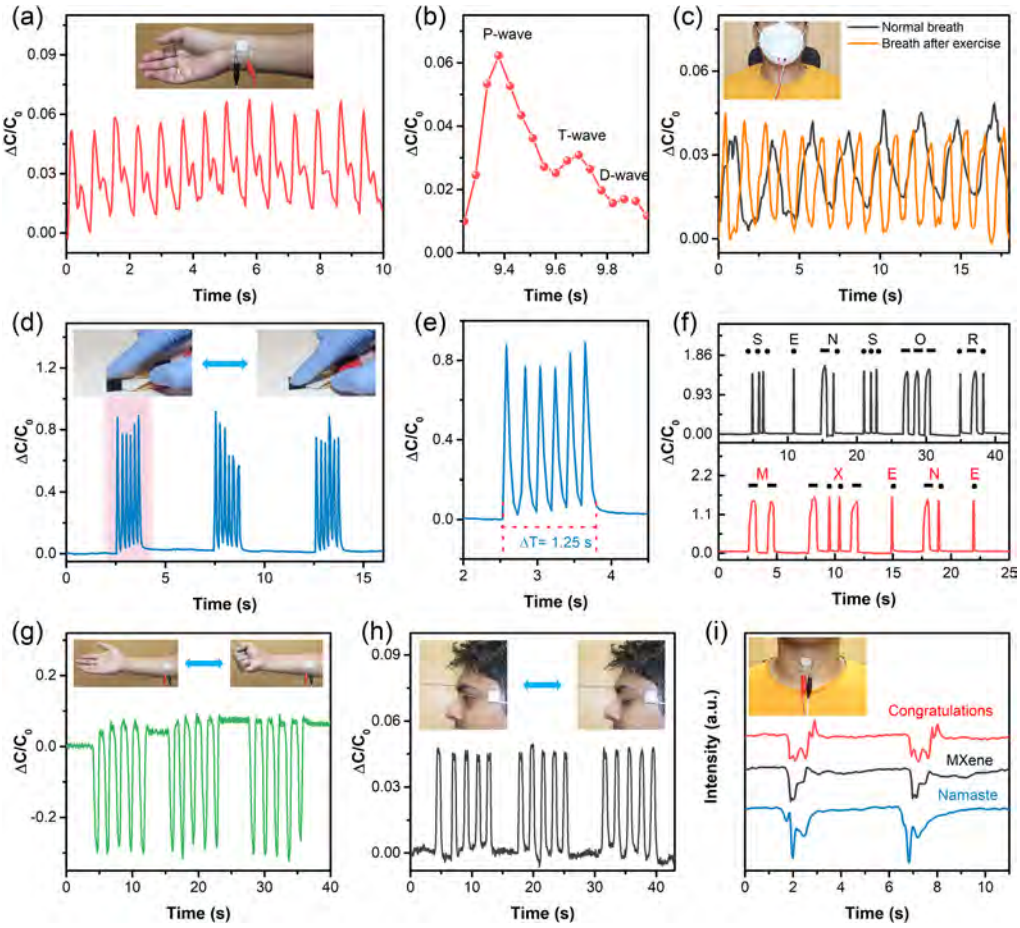


**Figure 6.** Application of the CNS-based sensor for the continuous and real-time monitoring of human physiological signals. (a) Real-time monitoring of the radial artery pulse wave. Inset: a photograph of the sensor attached to the wrist's dermal area. (b) Enlarged view of a single pulse waveform with the details of its characteristic peaks. (c) Respiration monitoring under pre- and post-exercise conditions. Inset: A photograph of the sensor attached to a mask for monitoring respiratory rate. (d) Illustration of the sensor's ability to mimic finger knocking for the detection of initial-stage Parkinson's disease at a static tremor frequency of 4.8 Hz. Insets: Photographs of the mimicked finger knocking on the sensor surface at a constant frequency. (e) Magnified view of the mimicked tapping at a specific tremor frequency of 4.8 Hz. (f) Generation of international Morse code signals from the sensor by short pressing and long pressing on the sensor. (g) Monitoring the muscle contraction−expansion via reversibly opening and closing a fist. Insets: Photographs of the sensor attached to a ventral arm muscle. (h) Monitoring of signals obtained from ocular muscle vibrations produced during eye twitching. Insets: Photographs of the sensor attached conformally near to an eye dermal area. (i) Ability of the sensor to recognize different phonations with repeatable and distinct waveforms. Inset: A photograph of the sensor attached to the superficial dermal layer of the throat.

published reports (Figure 4i and Table S1, Supporting Information) and shows that our CNS-based sensor has a lower detection limit and higher sensitivity than those reported by other articles.

The CNS-based sensor was subjected to different loading cycles in the low-pressure range, as shown in Figure 5a. The capacitive response of the sensor ($\Delta C/C_0$) in the low-pressure range is well correlated with the input pressure. The sensor can be smoothly operated in a very low-pressure range without noticeable noise or hysteresis, which affirms the ability of the sensor to detect subtle pressure changes. Figure 5b displays the ultralight-weight object detection capability of the CNS-based sensor; the fabricated sensor was able to detect 1.5 Pa, which is equivalent to single long rice grain (38 mg) on the sensor surface area ($1.5 \times 1.5$ cm$^2$). Furthermore, the sensor response for the sequential loading of the rice grain is also demonstrated in Figure 5b, which confirms the reliable detection of the ultralight-weight object. The CNS-based sensor exhibited excellent stability and durability of 10,000 loading and unloading cycle test under a high pressure of 167 kPa, as shown in Figure 5c. The left and right insets are the enlarged views of a few selected cycles, taken from the start and end of the test. From the insets, it can be noticed that the actual deterioration and hysteresis of the CNS are negligible even under a high-pressure (167 kPa) in comparison to those presented in recently published articles,[2,27,52] confirming that the CNS-based sensor has superior stability and long-term functioning capability.

**2.5. Human Physiology Monitoring.** Based on its outstanding performances, the sensor's applications in the real-time monitoring of human physiological signals for medical diagnosis were successfully demonstrated. The CNS-based sensor shows excellent potential in recognizing physiological signals acquired from the human wrist, as shown in Figure 6a. The inset reveals that the flexible sensor is conformally attached to a ventral side of the wrist's dermal area (30-years-old healthy volunteer) using medical tape. The pulse rate obtained from a human subject under normal conditions was 82 beats per minute, the complete range of radial pulses is displayed in Figure S11, Supporting


https://dx.doi.org/10.1021/acsami.0c05819
ACS Appl. Mater. Interfaces 2020, 12, 22212−22224

Information. Such a distinct and delicate recognition of the radial pulse by the CNS-based sensor exhibits its usefulness as a wearable clinical diagnostic device for identifying cardiovascular diseases by monitoring heart rate and rhythm. A magnified view of the waveform of the pulse signal is illustrated in Figure 6b, where the characteristic peaks D-wave, T-wave, and P-wave of a pulse waveform correspond to diastolic, tidal, and percussion responses, respectively. Arterial stiffness and abnormalities in the heart rhythm of a person can be identified by analyzing these three important peaks.[80] The CNS-based sensor can also precisely identify the pre-exercise and post-exercise breathing of a person, as depicted in Figure 6c. As depicted in the inset, the sensor is attached to a mask for monitoring the respiratory rate (breathing) of a volunteer (30-years-old, healthy volunteer). The normal and fast respiration rates were monitored, and they provide 24 and 48 respiration cycles per minute, respectively. This capability of the CNS-based sensor in the continuous and reliable detection of human respiration allows a person to monitor and detect any alterations in respiration, which can be an early sign of a serious respiratory illness, such as asthma, emphysema, bronchitis, sleep apnea, and so forth. Furthermore, the CNS-based sensor is capable of monitoring low-frequency changes by tapping on the sensor at an applicable frequency, which may diagnose the early onset of Parkinson's disease with presenting signs such as pill-rolling tremors or resting tremors (Figure 6d and its insets). In the early onset of Parkinson's disease, patients have an unnoticeable resting tremor in the hand that is normally at a frequency of 4−6 Hz, and the detection of this tremor sign is crucial for early diagnosis. Figure 6e is the magnified view of a finger with tremor at 4.8 Hz on the sensor, which reveals that the CNS-based sensor can be a potential candidate for the detection of an early sign of Parkinson's disease.[4] In addition, the sensor can be reliably used as a practical application for people with a variety of disabilities to communicate by generating a sequence of on−off signals such as (international Morse code) from finger knocking, for example, "sensor" and "MXene", as demonstrated in Figure 6f. In the Morse code technique, English letters are represented by the combination of short marks (dots) and long marks (dashes). The intermark gaps (dots and dashes) are usually made with one-dot duration, and inter-letter gaps are maintained with a three-dot duration, where dots and dashes correspond to short and long presses on the sensor. This sensor can be used as a medical device for patients having limitations on voluntary movements or paralyzed patients (such as Todd's paralysis, Brown-Sequard syndrome, Tetraplegia, etc.) to obtain responses or to express their feelings and emotions by tapping their finger on the sensor using the Morse code method. The CNS-based sensor was conformally attached to a ventral arm muscle to monitor the muscle contraction *via* reversibly opening and closing of a fist, as shown in the insets of Figure 6g. Monitoring muscle activities are extremely critical for the early diagnosis of musculoskeletal disorder, which is mainly caused by aging. In 2010, it was reported that approximately 6.7% of global death in the elderly population is caused by musculoskeletal disorders.[81] The CNS-based sensor can be applied for monitoring muscle movement to determine the healing process during any clinical surgery period with elderly and physically dysfunctional patients. Furthermore, the CNS-based sensor provides a perfect platform for the frequent monitoring of musculoskeletal-related parameters, which helps in early-onset diagnoses or progress reports by comparing signal peaks, obtained a few days ago and the present time. As shown in Figure 6g, the capacitance change is increased sharply in the reverse direction (negative $\Delta C/C_0$) due to the contraction of the ventral arm muscle. The CNS-based sensor shows an excellent ability to detect an ocular muscle vibration produced during eye twitching, as demonstrated in Figure 6h. The insets show the sensor attached near the eye of a volunteer. As the vibration is very subtle, a relative change in capacitance is less compared to that of other large deformations. Abnormal eyelid spasms can be a serious symptom of brain and nerve disorders (Parkinson's disease, Tourette's syndrome, and multiple sclerosis), so continuously monitoring the eyelid spasms of the subject can be beneficial for the early detection and diagnosis of these kinds of critical diseases.

The sensor exhibits a remarkable potential for voice recognition and can be used in the future as a human−machine interfacing device. The sensor was attached to the superficial dermal layer of the throat, as shown in the inset of Figure 6i. The output of the sensor produces distinct patterns for the pronunciation of different words, for example, "congratulations", "MXene" and "namaste", as demonstrated in Figure 6i. The sensor can identify minute vibration changes from the epidermis layer of a throat creating distinct signal patterns based on different phonation levels. Each word was tested twice to ensure the perfect repeatability of the sensor for voice recognition. Furthermore, to analyze the performance of the sensor in the influence of different bending angles, the sensor was subjected to different curvatures (0.2, 0.4, and 0.5 $cm^{-1}$, respectively), and corresponding capacitance responses were recorded, as shown in Figure S12, Supporting Information. The sensor subjected to a larger curvature shows the higher change in capacitance because of a greater bending angle compared with a smaller curvature.

## 3. CONCLUSIONS

In conclusion, we fabricated a highly sensitive, stable, and reliable CNS-based CPS *via* a large-scale and facile approach, characterized its electromechanical and electrical properties, and demonstrated its possibilities for diseases diagnosing and healthcare monitoring. The high-performance sensor was simply assembled by incorporating the MXene into the PVDF-TrFE nanofiber scaffolds and sandwiching it in between PEDOT:PSS/PDMS electrodes. In comparison with all of the fabricated sensors, the CNS with the 5% MXene concentration presented a better performance in terms of sensitivity and low-pressure detection. Because of the higher change in dielectric constant and low compression modulus of the CNS, the fabricated sensor exhibited good electromechanical performance, including ultra-low detection limit (1.5 Pa), wide pressure range up to 400 kPa, and excellent stability (>10,000 cycles under high-pressure of ∼167 kPa), suggesting highly reliable and long-term functioning capability of the device for the detection of ultra-low to large deformations. Based on the incredible performance of the sensor, subtle physiological signals generated from a human body were monitored (pulse rate, respiration, muscle movements, and eye twitching). We project that the CNS-based sensor can be reliably used as a wearable healthcare device for continuous monitoring and for prognosticating the health condition of patients.


https://dx.doi.org/10.1021/acsami.0c05819
ACS Appl. Mater. Interfaces 2020, 12, 22212−22224

## 4. MATERIALS AND METHODS

**4.1. Synthesis of MXene.** $Ti_3AlC_2$ powder was purchased from Carbon-Ukraine Ltd. Lithium fluoride (LiF) (>99.99% trace metals basis), and hydrochloric acid (HCl) (technical grade, 11.65 M) were obtained from Sigma-Aldrich. The synthesis of MXene ($Ti_3C_2T_x$) was carried out by a minimally intensive layer delamination method, which involved the selective etching of aluminum layers from its precursor $Ti_3AlC_2$. First, 1 g of LiF was added to 20 mL of 9 M HCl, and the solution was stirred for 5 min; this was followed by adding 1 g of $Ti_3AlC_2$ powder slowly and stirring for 24 h. The solution was washed repeatedly with deionized (DI) water *via* centrifugation (4000 rpm for 5 min) until its pH was neutralized at ∼6. Then, the obtained dark-green supernatant was combined with DI water and sonicated in an ice bath for 1 h to delaminate the MXene flakes, followed by 12 min centrifugation (8000 rpm). The stable dark green sediment was extracted and dried overnight at 50 °C using a convection oven to obtain MXene in the form of fine powder.

**4.2. Preparation of CNSs.** The properly dried MXene powder in *N*,*N*-dimethylformamide (DMF) was probe sonicated for 1 h at an amplitude of 100% to form a homogeneously dispersed suspension. Subsequently, the solution was centrifuged at 800 rpm for 15 min. The collected sediment was added to a 21% (w/w) PVDF-TrFE in DMF/ACT (3:2) solution to produce different MXene concentrations of up to 13 wt % and stirred for 3 h. Then, the solution was loaded into a 10 mL plastic syringe connected to a 21 gauge needle for electrospinning. The polymer solution was injected with a continuous flow rate of 2 mL $h^{-1}$ by applying a 20 kV potential over a collector-needle distance of 15 cm. All samples were electrospun with constant parameters, over a spinning area (5 × 5 $cm^2$) and in a controlled environment.

**4.3. Sensor Fabrication.** The CNS-based sensor was fabricated with a layer-by-layer stacking process. First, PDMS was prepared in a mixing ratio of base to cross-linker of 10:1 and spin-coated on a glass slide (5 × 5 cm) at 600 rpm for 60 s, followed by curing for 40 min. Subsequently, a 5 mL PEDOT:PSS solution (Clevios PH1000) was mixed with 5% (v/v) ethylene glycol and 1% (v/v) DVS, which were purchased from Sigma-Aldrich. The solution was stirred for 30 min before being spin-coated (1000 rpm for 60 s) on the surface of a cured PDMS that had received an $O_2$ plasma treatment (150 W, 10 s). After spin-coating, the film was kept on a hot plate for 60 min at 60 °C for drying. To increase the conductivity, the film was post-treated with DMSO and dried inside a convection oven for 15 min. The PEDOT:PSS electrode film with the PDMS was peeled off from the glass substrate, and the sheet resistance of the as-prepared film was measured using a four-point probe meter (RCD3175, EDTM). The prepared CNS was inserted in between two PEDOT:PSS electrodes facing opposite each other. Finally, two flexible, highly conductive carbon tape electrodes were attached to the top and bottom PEDOT:PSS films.

**4.4. Characterization.** The structure and morphology of the nanofibers were characterized by FESEM (JSM-6700F). EDS, for the elemental dispersion analysis, was performed with the same instrument. Raman spectroscopy was performed by a Renishaw to study the different vibration modes and lattice deformation behavior of molecules in the MXene. XPS was performed using a PHI 5000 VersaProbe (Ulvac-PHI, Japan) for a more detailed analysis of the chemical state, bonding, and composition of the composite material and MXene. The crystallographic structure of the composite fibers was measured by XRD. FTIR was conducted using a Thermo Scientific NICOLETiS10 for the characterization of different-concentration composite samples. For electromechanical characterization, a moving machine (JSV-H1000, Japan Instrumentation System Co., Ltd.) connected with a force gauge (HF-1, Japan Instrumentation System Co., Ltd.) was used to apply a precise static and dynamic load, which has quantified by variable compression distance employed to the sensor by manual programming. An acrylic spacer of 2 cm × 2 cm was used between the force gauge fixture and the sensor for applying a uniform compressive load. Similarly, the electrical parameters (capacitance, resistance, phase, conductivity, dielectric constant, and dielectric loss) were recorded using an LCR meter (Hioki, IM 3536) with an ac voltage of 1 V at 1 kHz.

## ■ ASSOCIATED CONTENT

### Supporting Information

The Supporting Information is available free of charge at https://pubs.acs.org/doi/10.1021/acsami.0c05819.

Preparation of the PEDOT:PSS/PDMS thin film, measurement of sheet resistance, TEM analysis, cross-sectional FESEM image of MXene, XRD diffraction and Raman spectroscopy of the Ti3C2Tx MXene nanosheet, XRD spectra and XPS spectra of MXene/PVDF-TrFE, dielectric loss and conductivity of CNS, complete range of radial artery pulse wave, sensor influence under different bending condition and performance comparison of the various pressure sensor (PDF)

## ■ AUTHOR INFORMATION


### Corresponding Author

**Jae Yeong Park** − *Department of Electronic Engineering, Kwangwoon University, Seoul 01897, Republic of Korea;* orcid.org/0000-0002-2056-5151; Email: jaepark@kw.ac.kr

### Authors

**Sudeep Sharma** − *Department of Electronic Engineering, Kwangwoon University, Seoul 01897, Republic of Korea*

**Ashok Chhetry** − *Department of Electronic Engineering, Kwangwoon University, Seoul 01897, Republic of Korea*

**Md Sharifuzzaman** − *Department of Electronic Engineering, Kwangwoon University, Seoul 01897, Republic of Korea*

**Hyosang Yoon** − *Department of Electronic Engineering, Kwangwoon University, Seoul 01897, Republic of Korea*

Complete contact information is available at: https://pubs.acs.org/10.1021/acsami.0c05819


### Author Contributions

S.S. conceived the idea, fabricated, characterized the device and wrote the manuscript. A.C. assisted with device characterization and measurements. M.S. and H.Y. assisted for analytical characterizations, and J.Y.P. provided research guidance. All the authors have approved the final version of the manuscript.

### Notes

The authors declare no competing financial interest.

## ■ ACKNOWLEDGMENTS

This research was supported by the Bio & Medical Technology Development Program of the NRF grant funded by the Korean government (MSIT) (NRF-2017M3A9F1031270). Besides, the authors are grateful to the Micro/Nano Devices and Packaging (MiNDaP) Lab group members of Kwangwoon University for their valuable suggestion and support.

## ■ REFERENCES

(1) Son, D.; Bao, Z. Nanomaterials in Skin-Inspired Electronics: Toward Soft and Robust Skin-like Electronic Nanosystems. *ACS Nano* **2018**, *12*, 11731−11739.

(2) Zhan, Z.; Lin, R.; Tran, V.-T.; An, J.; Wei, Y.; Du, H.; Tran, T.; Lu, W. Paper/Carbon Nanotube-Based Wearable Pressure Sensor for Physiological Signal Acquisition and Soft Robotic Skin. *ACS Appl. Mater. Interfaces* **2017**, *9*, 37921−37928.

(3) Cho, S.; Kang, S.; Pandya, A.; Shanker, R.; Khan, Z.; Lee, Y.; Park, J.; Craig, S. L.; Ko, H. Large-Area Cross-Aligned Silver

Nanowire Electrodes for Flexible, Transparent, and Force-Sensitive Mechanochromic Touch Screens. *ACS Nano* **2017**, *11*, 4346−4357.
(4) Guo, Y.; Zhong, M.; Fang, Z.; Wan, P.; Yu, G. A Wearable Transient Pressure Sensor Made with MXene Nanosheets for Sensitive Broad-Range Human-Machine Interfacing. *Nano Lett.* **2019**, *19*, 1143−1150.
(5) Kang, M.; Kim, J.; Jang, B.; Chae, Y.; Kim, J.-H.; Ahn, J.-H. Graphene-Based Three-Dimensional Capacitive Touch Sensor for Wearable Electronics. *ACS Nano* **2017**, *11*, 7950−7957.
(6) Chhetry, A.; Yoon, H.; Park, J. Y. A Flexible and Highly Sensitive Capacitive Pressure Sensor Based on Conductive Fibers with a Microporous Dielectric for Wearable Electronics. *J. Mater. Chem. C* **2017**, *5*, 10068−10076.
(7) Lee, J.; Kwon, H.; Seo, J.; Shin, S.; Koo, J. H.; Pang, C.; Son, S.; Kim, J. H.; Jang, Y. H.; Kim, D. E.; et al. Conductive Fiber-Based Ultrasensitive Textile Pressure Sensor for Wearable Electronics. *Adv. Mater.* **2015**, *27*, 2433−2439.
(8) Lin, L.; Xie, Y.; Wang, S.; Wu, W.; Niu, S.; Wen, X.; Wang, Z. L. Triboelectric Active Sensor Array for Self-Powered Static and Dynamic Pressure Detection and Tactile Imaging. *ACS Nano* **2013**, *7*, 8266−8274.
(9) Tewari, A.; Gandla, S.; Bohm, S.; McNeill, C. R.; Gupta, D. Highly Exfoliated MWNT-RGO Ink-Wrapped Polyurethane Foam for Piezoresistive Pressure Sensor Applications. *ACS Appl. Mater. Interfaces* **2018**, *10*, 5185−5195.
(10) Yao, H.-B.; Ge, J.; Wang, C.-F.; Wang, X.; Hu, W.; Zheng, Z.-J.; Ni, Y.; Yu, S.-H. A Flexible and Highly Pressure-Sensitive Graphene-Polyurethane Sponge Based on Fractured Microstructure Design. *Adv. Mater.* **2013**, *25*, 6692−6698.
(11) He, W.; Li, G.; Zhang, S.; Wei, Y.; Wang, J.; Li, Q.; Zhang, X. Polypyrrole/Silver Coaxial Nanowire Aero-Sponges for Temperature-Independent Stress Sensing and Stress-Triggered Joule Heating. *ACS Nano* **2015**, *9*, 4244−4251.
(12) Chen, Z.; Wang, Z.; Li, X.; Lin, Y.; Luo, N.; Long, M.; Zhao, N.; Xu, J.-B. Flexible Piezoelectric-Induced Pressure Sensors for Static Measurements Based on Nanowires/Graphene Heterostructures. *ACS Nano* **2017**, *11*, 4507−4513.
(13) Liu, S.; Wang, L.; Wang, Z.; Cai, Y.; Feng, X.; Qin, Y.; Wang, Z. L. Double-Channel Piezotronic Transistors for Highly Sensitive Pressure Sensing. *ACS Nano* **2018**, *12*, 1732−1738.
(14) Phan, H.-P.; Zhong, Y.; Nguyen, T.-K.; Park, Y.; Dinh, T.; Song, E.; Vadivelu, R. K.; Masud, M. K.; Li, J.; Shiddiky, M. J. A.; et al. Long-Lived, Transferred Crystalline Silicon Carbide Nanomembranes for Implantable Flexible Electronics. *ACS Nano* **2019**, *13*, 11572−11581.
(15) Tolvanen, J.; Hannu, J.; Jantunen, H. Hybrid Foam Pressure Sensor Utilizing Piezoresistive and Capacitive Sensing Mechanisms. *IEEE Sens. J.* **2017**, *17*, 4735−4746.
(16) Yin, X.; Vinod, T. P.; Jelinek, R. A Flexible High-Sensitivity Piezoresistive Sensor Comprising a Au Nanoribbon-Coated Polymer Sponge. *J. Mater. Chem. C* **2015**, *3*, 9247−9252.
(17) Wu, X.; Han, Y.; Zhang, X.; Zhou, Z.; Lu, C. Large-Area Compliant, Low-Cost, and Versatile Pressure-Sensing Platform Based on Microcrack-Designed Carbon Black@Polyurethane Sponge for Human-Machine Interfacing. *Adv. Funct. Mater.* **2016**, *26*, 6246−6256.
(18) Wu, Y.-h.; Liu, H.-z.; Chen, S.; Dong, X.-c.; Wang, P.-p.; Liu, S.-q.; Lin, Y.; Wei, Y.; Liu, L. Channel Crack-Designed Gold@PU Sponge for Highly Elastic Piezoresistive Sensor with Excellent Detectability. *ACS Appl. Mater. Interfaces* **2017**, *9*, 20098−20105.
(19) Khalid, M. A. U.; Ali, M.; Soomro, A. M.; Kim, S. W.; Kim, H. B.; Lee, B.-G.; Choi, K. H. A Highly Sensitive Biodegradable Pressure Sensor Based on Nanofibrous Dielectric. *Sens. Actuators, A* **2019**, *294*, 140−147.
(20) Kim, J.; Nga Ng, T.; Soo Kim, W. Highly Sensitive Tactile Sensors Integrated with Organic Transistors. *Appl. Phys. Lett.* **2012**, *101*, 103308.
(21) Luo, Y.; Shao, J.; Chen, S.; Chen, X.; Tian, H.; Li, X.; Wang, L.; Wang, D.; Lu, B. Flexible Capacitive Pressure Sensor Enhanced by Tilted Micropillar Arrays. *ACS Appl. Mater. Interfaces* **2019**, *11*, 17796−17803.
(22) Guo, Y.; Gao, S.; Yue, W.; Zhang, C.; Li, Y. Anodized Aluminum Oxide-Assisted Low-Cost Flexible Capacitive Pressure Sensors Based on Double-Sided Nanopillars by a Facile Fabrication Method. *ACS Appl. Mater. Interfaces* **2019**, *11*, 48594−48603.
(23) Boutry, C. M.; Nguyen, A.; Lawal, Q. O.; Chortos, A.; Rondeau-Gagné, S.; Bao, Z. A Sensitive and Biodegradable Pressure Sensor Array for Cardiovascular Monitoring. *Adv. Mater.* **2015**, *27*, 6954−6961.
(24) Wang, X.; Dong, L.; Zhang, H.; Yu, R.; Pan, C.; Wang, Z. L. Recent Progress in Electronic Skin. *Adv. Sci.* **2015**, *2*, 1500169.
(25) Ruth, S. R. A.; Beker, L.; Tran, H.; Feig, V. R.; Matsuhisa, N.; Bao, Z. Rational Design of Capacitive Pressure Sensors Based on Pyramidal Microstructures for Specialized Monitoring of Biosignals. *Adv. Funct. Mater.* **2019**, *1903100*, 1−12.
(26) Mannsfeld, S. C. B.; Tee, B. C.-K.; Stoltenberg, R. M.; Chen, C. V. H.-H.; Barman, S.; Muir, B. V. O.; Sokolov, A. N.; Reese, C.; Bao, Z. Highly Sensitive Flexible Pressure Sensors with Microstructured Rubber Dielectric Layers. *Nat. Mater.* **2010**, *9*, 859−864.
(27) Chhetry, A.; Kim, J.; Yoon, H.; Park, J. Y. Ultrasensitive Interfacial Capacitive Pressure Sensor Based on a Randomly Distributed Microstructured Iontronic Film for Wearable Applications. *ACS Appl. Mater. Interfaces* **2019**, *11*, 3438−3449.
(28) Wang, Q.; Jian, M.; Wang, C.; Zhang, Y. Carbonized Silk Nanofiber Membrane for Transparent and Sensitive Electronic Skin. *Adv. Funct. Mater.* **2017**, *27*, 1605657.
(29) Matsumoto, H.; Tanioka, A. Functionality in Electrospun Nanofibrous Membranes Based on Fiber's Size, Surface Area, and Molecular Orientation. *Membranes* **2011**, *1*, 249−264.
(30) Ko, F. K.; Wan, Y. *Introduction to Nanofiber Materials*; Cambridge University Press, 2014; pp 1−267.
(31) Kenry; Lim, C. T. Nanofiber technology: current status and emerging developments. *Prog. Polym. Sci.* **2017**, *70*, 1−17.
(32) Chinnappan, A.; Baskar, C.; Baskar, S.; Ratheesh, G.; Ramakrishna, S. An Overview of Electrospun Nanofibers and Their Application in Energy Storage, Sensors and Wearable/Flexible Electronics. *J. Mater. Chem. C* **2017**, *5*, 12657−12673.
(33) Otto, W. H. Relationship of Tensile Strength of Glass Fibers to Diameter. *J. Am. Ceram. Soc.* **2006**, *38*, 122−125.
(34) Sobolčiak, P.; Ali, A.; Hassan, M. K.; Helal, M. I.; Tanvir, A.; Popelka, A.; Al-Maadeed, M. A.; Krupa, I.; Mahmoud, K. A. 2D Ti3C2Tx (MXene)-Reinforced Polyvinyl Alcohol (PVA) Nanofibers with Enhanced Mechanical and Electrical Properties. *PLoS One* **2017**, *12*, e0183705.
(35) Levitt, A. S.; Alhabeb, M.; Hatter, C. B.; Sarycheva, A.; Dion, G.; Gogotsi, Y. Electrospun MXene/Carbon Nanofibers as Supercapacitor Electrodes. *J. Mater. Chem. A* **2019**, *7*, 269−277.
(36) Tu, S.; Jiang, Q.; Zhang, X.; Alshareef, H. N. Large Dielectric Constant Enhancement in MXene Percolative Polymer Composites. *ACS Nano* **2018**, *12*, 3369−3377.
(37) Cao, Y.; Deng, Q.; Liu, Z.; Shen, D.; Wang, T.; Huang, Q.; Du, S.; Jiang, N.; Lin, C.-T.; Yu, J. Enhanced Thermal Properties of Poly(Vinylidene Fluoride) Composites with Ultrathin Nanosheets of MXene. *RSC Adv.* **2017**, *7*, 20494−20501.
(38) Chen, S.; Han, D.; Hou, H. High Strength Electrospun Fibers. *Polym. Adv. Technol.* **2011**, *22*, 295−303.
(39) Beese, A. M.; Sarkar, S.; Nair, A.; Naraghi, M.; An, Z.; Moravsky, A.; Loutfy, R. O.; Buehler, M. J.; Nguyen, S. T.; Espinosa, H. D. Bio-Inspired Carbon Nanotube-Polymer Composite Yarns with Hydrogen Bond-Mediated Lateral Interactions. *ACS Nano* **2013**, *7*, 3434−3446.
(40) Daghigh, H.; Daghigh, V. Free vibration of size and temperature-dependent carbon nanotube (CNT)-reinforced composite nanoplates with CNT agglomeration. *Polym. Compos.* **2019**, *40*, E1479−E1494.
(41) Liao, Y.; Zhang, C.; Zhang, Y.; Strong, V.; Tang, J.; Li, X.-G.; Kalantar-Zadeh, K.; Hoek, E. M. V.; Wang, K. L.; Kaner, R. B. Carbon


https://dx.doi.org/10.1021/acsami.0c05819
*ACS Appl. Mater. Interfaces* 2020, 12, 22212−22224

Nanotube/Polyaniline Composite Nanofibers: Facile Synthesis and Chemosensors. *Nano Lett.* **2011**, *11*, 954−959.
(42) Zhong, W.; Liu, C.; Liu, Q.; Piao, L.; Jiang, H.; Wang, W.; Liu, K.; Li, M.; Sun, G.; Wang, D. Ultrasensitive Wearable Pressure Sensors Assembled by Surface-Patterned Polyolefin Elastomer Nanofiber Membrane Interpenetrated with Silver Nanowires. *ACS Appl. Mater. Interfaces* **2018**, *10*, 42706−42714.
(43) Wen, J.; Tan, X.; Hu, Y.; Guo, Q.; Hong, X. Filtration and Electrochemical Disinfection Performance of PAN/PANI/AgNWs-CC Composite Nanofiber Membrane. *Environ. Sci. Technol.* **2017**, *51*, 6395−6403.
(44) Zhang, S.; Ni, W.; Kou, X.; Yeung, M. H.; Sun, L.; Wang, J.; Yan, C. Formation of Gold and Silver Nanoparticle Arrays and Thin Shells on Mesostructured Silica Nanofibers. *Adv. Funct. Mater.* **2007**, *17*, 3258−3266.
(45) Wu, Q.; Xu, Y.; Yao, Z.; Liu, A.; Shi, G. Supercapacitors Based on Flexible Graphene/Polyaniline Nanofiber Composite Films. *ACS Nano* **2010**, *4*, 1963−1970.
(46) Kwon, S. R.; Harris, J.; Zhou, T.; Loufakis, D.; Boyd, J. G.; Lutkenhaus, J. L. Mechanically Strong Graphene/Aramid Nanofiber Composite Electrodes for Structural Energy and Power. *ACS Nano* **2017**, *11*, 6682−6690.
(47) Ren, H.; Zheng, L.; Wang, G.; Gao, X.; Tan, Z.; Shan, J.; Cui, L.; Li, K.; Jian, M.; Zhu, L.; et al. Transfer-Medium-Free Nanofiber-Reinforced Graphene Film and Applications in Wearable Transparent Pressure Sensors. *ACS Nano* **2019**, *13*, 5541−5548.
(48) Cao, W.-T.; Chen, F.-F.; Zhu, Y.-J.; Zhang, Y.-G.; Jiang, Y.-Y.; Ma, M.-G.; Chen, F. Binary Strengthening and Toughening of MXene/Cellulose Nanofiber Composite Paper with Nacre-Inspired Structure and Superior Electromagnetic Interference Shielding Properties. *ACS Nano* **2018**, *12*, 4583−4593.
(49) Mayerberger, E. A.; Urbanek, O.; McDaniel, R. M.; Street, R. M.; Barsoum, M. W.; Schauer, C. L. Preparation and characterization of polymer-Ti3C2Tx(MXene) composite nanofibers produced via electrospinning. *J. Appl. Polym. Sci.* **2017**, *134*, 45295.
(50) Shao, W.; Tebyetekerwa, M.; Marriam, I.; Li, W.; Wu, Y.; Peng, S.; Ramakrishna, S.; Yang, S.; Zhu, M. Polyester@MXene Nanofibers-Based Yarn Electrodes. *J. Power Sources* **2018**, *396*, 683−690.
(51) Behler, K. D.; Stravato, A.; Mochalin, V.; Korneva, G.; Yushin, G.; Gogotsi, Y. Nanodiamond-Polymer Composite Fibers and Coatings. *ACS Nano* **2009**, *3*, 363−369.
(52) Mu, C.; Li, J.; Song, Y.; Huang, W.; Ran, A.; Deng, K.; Huang, J.; Xie, W.; Sun, R.; Zhang, H. Enhanced Piezocapacitive Effect in CaCu3Ti4O12-Polydimethylsiloxane Composited Sponge for Ultra-sensitive Flexible Capacitive Sensor. *ACS Appl. Nano Mater.* **2018**, *1*, 274−283.
(53) Liu, M.; Pu, X.; Jiang, C.; Liu, T.; Huang, X.; Chen, L.; Du, C.; Sun, J.; Hu, W.; Wang, Z. L. Large-Area All-Textile Pressure Sensors for Monitoring Human Motion and Physiological Signals. *Adv. Mater.* **2017**, *29*, 1703700.
(54) Naguib, M.; Kurtoglu, M.; Presser, V.; Lu, J.; Niu, J.; Heon, M.; Hultman, L.; Gogotsi, Y.; Barsoum, M. W. Two-Dimensional Nanocrystals Produced by Exfoliation of Ti3AlC2. *Adv. Mater.* **2011**, *23*, 4248−4253.
(55) Alhabeb, M.; Maleski, K.; Anasori, B.; Lelyukh, P.; Clark, L.; Sin, S.; Gogotsi, Y. Guidelines for Synthesis and Processing of Two-Dimensional Titanium Carbide (Ti3C2Tx MXene). *Chem. Mater.* **2017**, *29*, 7633−7644.
(56) Lukatskaya, M. R.; Kota, S.; Lin, Z.; Zhao, M. Q.; Shpigel, N.; Levi, M. D.; Halim, J.; Taberna, P. L.; Barsoum, M. W.; Simon, P.; et al. Ultra-High-Rate Pseudocapacitive Energy Storage in Two-Dimensional Transition Metal Carbides. *Nat. Energy* **2017**, *2*, 17105.
(57) Lukatskaya, M. R.; Bak, S.-M.; Yu, X.; Yang, X.-Q.; Barsoum, M. W.; Gogotsi, Y. Probing the Mechanism of High Capacitance in 2D Titanium Carbide Using in Situ X-Ray Absorption Spectroscopy. *Adv. Energy Mater.* **2015**, *5*, 1500589.
(58) Rakhi, R. B.; Ahmed, B.; Hedhili, M. N.; Anjum, D. H.; Alshareef, H. N. Effect of Postetch Annealing Gas Composition on the Structural and Electrochemical Properties of $Ti_2CT_x$ MXene Electrodes for Supercapacitor Applications. *Chem. Mater.* **2015**, *27*, 5314−5323.
(59) Kim, S. J.; Koh, H.-J.; Ren, C. E.; Kwon, O.; Maleski, K.; Cho, S.-Y.; Anasori, B.; Kim, C.-K.; Choi, Y.-K.; Kim, J.; et al. Metallic Ti3C2Tx MXene Gas Sensors with Ultrahigh Signal-to-Noise Ratio. *ACS Nano* **2018**, *12*, 986−993.
(60) Shahzad, F.; Alhabeb, M.; Hatter, C. B.; Anasori, B.; Man Hong, S.; Koo, C. M.; Gogotsi, Y. Electromagnetic Interference Shielding with 2D Transition Metal Carbides (MXenes). *Science* **2016**, *353*, 1137−1140.
(61) Jiang, C.; Wu, C.; Li, X.; Yao, Y.; Lan, L.; Zhao, F.; Ye, Z.; Ying, Y.; Ping, J. All-Electrospun Flexible Triboelectric Nanogenerator Based on Metallic MXene Nanosheets. *Nano Energy* **2019**, *59*, 268−276.
(62) Jiang, X.-Z.; Sun, Y. J.; Fan, Z.; Zhang, T. Y. Integrated Flexible, Waterproof, Transparent, and Self-Powered Tactile Sensing Panel. *ACS Nano* **2016**, *10*, 7696−7704.
(63) Lee, J. H.; Yoon, H. J.; Kim, T. Y.; Gupta, M. K.; Lee, J. H.; Seung, W.; Ryu, H.; Kim, S. W. Micropatterned P(VDF-TrFE) Film-Based Piezoelectric Nanogenerators for Highly Sensitive Self-Powered Pressure Sensors. *Adv. Funct. Mater.* **2015**, *25*, 3203−3209.
(64) Fan, X.; Nie, W.; Tsai, H.; Wang, N.; Huang, H.; Cheng, Y.; Wen, R.; Ma, L.; Yan, F.; Xia, Y. PEDOT:PSS for Flexible and Stretchable Electronics: Modifications, Strategies, and Applications. *Adv. Sci.* **2019**, *6*, 1900813.
(65) Liu, S.; Yu, H.; Zhang, Q.; Qin, F.; Zhang, X.; Zhang, L.; Xie, W. Efficient ITO-Free Organic Light-Emitting Devices with Dual-Functional PSS-Rich PEDOT:PSS Electrode by Enhancing Carrier Balance. *J. Mater. Chem. C* **2019**, *7*, 5426−5432.
(66) Kayser, L. V.; Lipomi, D. J. Stretchable Conductive Polymers and Composites Based on PEDOT and PEDOT:PSS. *Adv. Mater.* **2019**, *31*, 1806133.
(67) Chou, T.-R.; Chen, S.-H.; Chiang, Y.-T.; Lin, Y.-T.; Chao, C.-Y. Highly Conductive PEDOT:PSS Film by Post-Treatment with Dimethyl Sulfoxide for ITO-Free Liquid Crystal Display. *Mol. Cryst. Liq. Cryst.* **2015**, *612*, 201−210.
(68) del Agua, I.; Mantione, D.; Ismailov, U.; Sanchez-Sanchez, A.; Aramburu, N.; Malliaras, G. G.; Mecerreyes, D.; Ismailova, E. DVS-Crosslinked PEDOT:PSS Free-Standing and Textile Electrodes toward Wearable Health Monitoring. *Adv. Mater. Technol.* **2018**, *3*, 1700322.
(69) Feng, W.; Luo, H.; Wang, Y.; Zeng, S.; Deng, L.; Zhou, X.; Zhang, H.; Peng, S. Ti3C2MXene: a promising microwave absorbing material. *RSC Adv.* **2018**, *8*, 2398−2403.
(70) Wu, J.-B.; Lin, M.-L.; Cong, X.; Liu, H.-N.; Tan, P.-H. Raman Spectroscopy of Graphene-Based Materials and Its Applications in Related Devices. *Chem. Soc. Rev.* **2018**, *47*, 1822−1873.
(71) Kumar, S.; Lei, Y.; Alshareef, N. H.; Quevedo-Lopez, M. A.; Salama, K. N. Biofunctionalized Two-Dimensional Ti3C2 MXenes for Ultrasensitive Detection of Cancer Biomarker. *Biosens. Bioelectron.* **2018**, *121*, 243−249.
(72) Zheng, J.; He, A.; Li, J.; Han, C. C. Polymorphism Control of Poly(Vinylidene Fluoride) through Electrospinning. *Macromol. Rapid Commun.* **2007**, *28*, 2159−2162.
(73) Zhang, Y.; Zhao, Y.; Tan, S.; Zhang, Z. Inserting -CHCH- into P(VDF-TrFE) by C-F Activation Mediated with Cu(0) in a Controlled Atom Transfer Radical Elimination Process. *Polym. Chem.* **2017**, *8*, 1840−1849.
(74) Li, W.; Song, Z.; Zhong, J.; Qian, J.; Tan, Z.; Wu, X.; Chu, H.; Nie, W.; Ran, X. Multilayer-Structured Transparent MXene/PVDF Film with Excellent Dielectric and Energy Storage Performance. *J. Mater. Chem. C* **2019**, *7*, 10371−10378.
(75) Lei, T.; Xue, Q.; Chu, L.; Han, Z.; Sun, J.; Xia, F.; Zhang, Z.; Guo, Q. Excellent Dielectric Properties of Polymer Composites Based on Core-Shell Structured Carbon/Silica Nanohybrid. *Appl. Phys. Lett.* **2013**, *103*, 012902.
(76) Nan, C.-W.; Shen, Y.; Ma, J. Physical Properties of Composites Near Percolation. *Annu. Rev. Mater. Res.* **2010**, *40*, 131−151.


https://dx.doi.org/10.1021/acsami.0c05819
ACS Appl. Mater. Interfaces 2020, 12, 22212−22224

(77) Yang, W.; Li, N.-W.; Zhao, S.; Yuan, Z.; Wang, J.; Du, X.; Wang, B.; Cao, R.; Li, X.; Xu, W.; et al. A Breathable and Screen-Printed Pressure Sensor Based on Nanofiber Membranes for Electronic Skins. *Adv. Mater. Technol.* **2018**, *3*, 1700241.
(78) Ansaloni, L.; Deng, L. *Advances in Polymer-Inorganic Hybrids as Membrane Materials*; Elsevier Ltd., 2016.
(79) Zhang, H.; Zhang, Z.; Friedrich, K.; Eger, C. Property Improvements of in Situ Epoxy Nanocomposites with Reduced Interparticle Distance at High Nanosilica Content. *Acta Mater.* **2006**, *54*, 1833−1842.
(80) Lee, Y.; Park, J.; Cho, S.; Shin, Y.-E.; Lee, H.; Kim, J.; Myoung, J.; Cho, S.; Kang, S.; Baig, C.; et al. Flexible Ferroelectric Sensors with Ultrahigh Pressure Sensitivity and Linear Response over Exceptionally Broad Pressure Range. *ACS Nano* **2018**, *12*, 4045−4054.
(81) Faisal, A. I.; Majumder, S.; Mondal, T.; Cowan, D.; Naseh, S.; Deen, M. J. Monitoring Methods of Human Body Joints: State-of-the-Art and Research Challenges. *Sensors* **2019**, *19*, 2629.


https://dx.doi.org/10.1021/acsami.0c05819
*ACS Appl. Mater. Interfaces* 2020, 12, 22212−22224